LETTER

doi:10.1038/nature25476

Processing bulk natural wood into a high-performance structural material

Jianwei Song[1]*, Chaoji Chen[1]*, Shuze Zhu[2]*, Mingwei Zhu[1]*, Jiaqi Dai[1], Upamanyu Ray[2], Yiju Li[1], Yudi Kuang[1], Yongfeng Li[1], Nelson Quispe[2], Yonggang Yao[1], Amy Gong[1], Ulrich H. Leiste[3], Hugh A. Bruck[2], J. Y. Zhu[4], Azhar Vellore[5], Heng Li[6], Marilyn L. Minus[6], Zheng Jia[2], Ashlie Martini[5], Teng Li[2] & Liangbing Hu[1]

Synthetic structural materials with exceptional mechanical performance suffer from either large weight and adverse environmental impact (for example, steels and alloys) or complex manufacturing processes and thus high cost (for example, polymer-based and biomimetic composites)[1–8]. Natural wood is a low-cost and abundant material and has been used for millennia as a structural material for building and furniture construction[9]. However, the mechanical performance of natural wood (its strength and toughness) is unsatisfactory for many advanced engineering structures and applications. Pre-treatment with steam, heat, ammonia or cold rolling[10–21] followed by densification has led to the enhanced mechanical performance of natural wood. However, the existing methods result in incomplete densification and lack dimensional stability, particularly in response to humid environments[14], and wood treated in these ways can expand and weaken. Here we report a simple and effective strategy to transform bulk natural wood directly into a high-performance structural material with a more than tenfold increase in strength, toughness and ballistic resistance and with greater dimensional stability. Our two-step process involves the partial removal of lignin and hemicellulose from the natural wood via a boiling process in an aqueous mixture of NaOH and Na_2SO_3 followed by hot-pressing, leading to the total collapse of cell walls and the complete densification of the natural wood with highly aligned cellulose nanofibres. This strategy is shown to be universally effective for various species of wood. Our processed wood has a specific strength higher than that of most structural metals and alloys, making it a low-cost, high-performance, lightweight alternative.

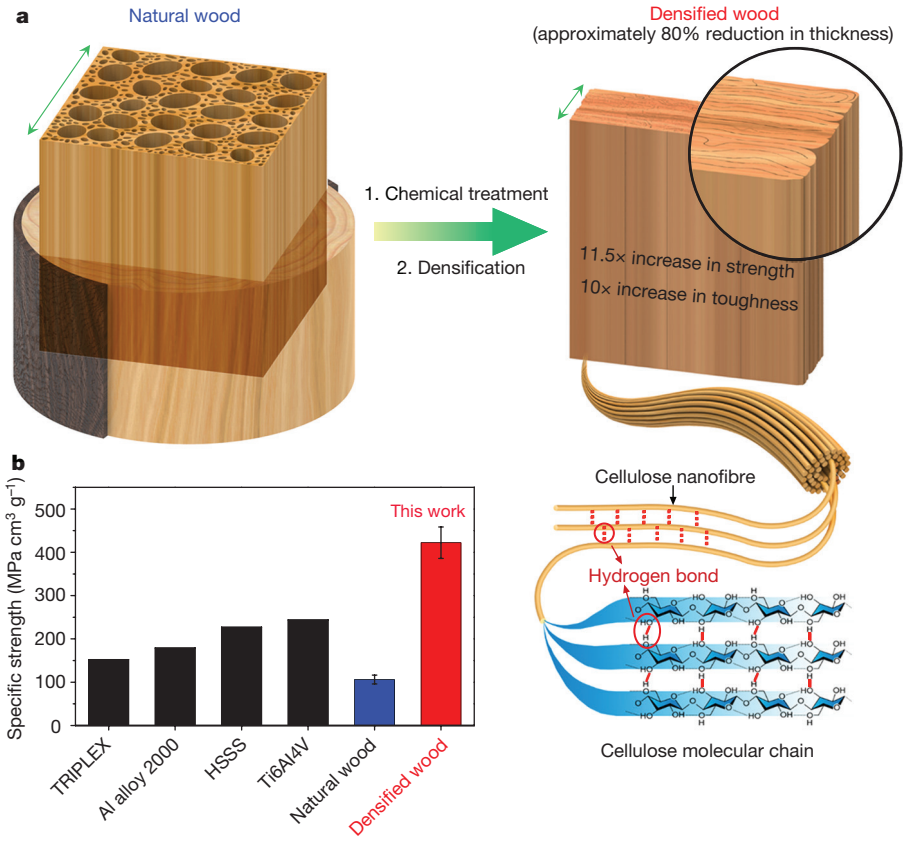

Figure 1 | Processing approach and mechanical performance of densified wood. a, Schematic of the top-down two-step approach to transforming bulk natural wood directly into super-strong and tough densified wood. Step 1, chemical treatment to partially remove lignin/hemicellulose; step 2, mechanical hot-pressing at 100 °C, which leads to a reduction in thickness of about 80%. Most of the densified wood consists of well aligned cellulose nanofibres, which greatly enhance hydrogen bond formation among neighbouring nanofibres. **b**, Specific tensile strength of the resulting densified wood (422.2 ± 36.3 MPa $cm^3 g^{-1}$, mean ± standard deviation) is shown to be higher than those of typical metals (the Fe-Al-Mn-C alloy, TRIPLEX and high-specific-strength steel, HSSS), and even of lightweight titanium alloy (Ti6Al4V). Error bars in Figs 1–4 and Extended Data Figs 1–10 show standard deviation with $n = 5$ repeats, unless noted otherwise.

[1]Department of Materials Science and Engineering, University of Maryland, College Park, Maryland 20742, USA. [2]Department of Mechanical Engineering, University of Maryland, College Park, Maryland 20742, USA. [3]Department of Aerospace Engineering, University of Maryland, College Park, Maryland 20742, USA. [4]Forest Products Laboratory, USDA Forest Service, Madison, Wisconsin 53726, USA. [5]Department of Mechanical Engineering, University of California Merced, Merced, California 95343, USA. [6]Department of Mechanical and Industrial Engineering, Northeastern University, Boston, Massachusetts 02115, USA.
*These authors contributed equally to this work.

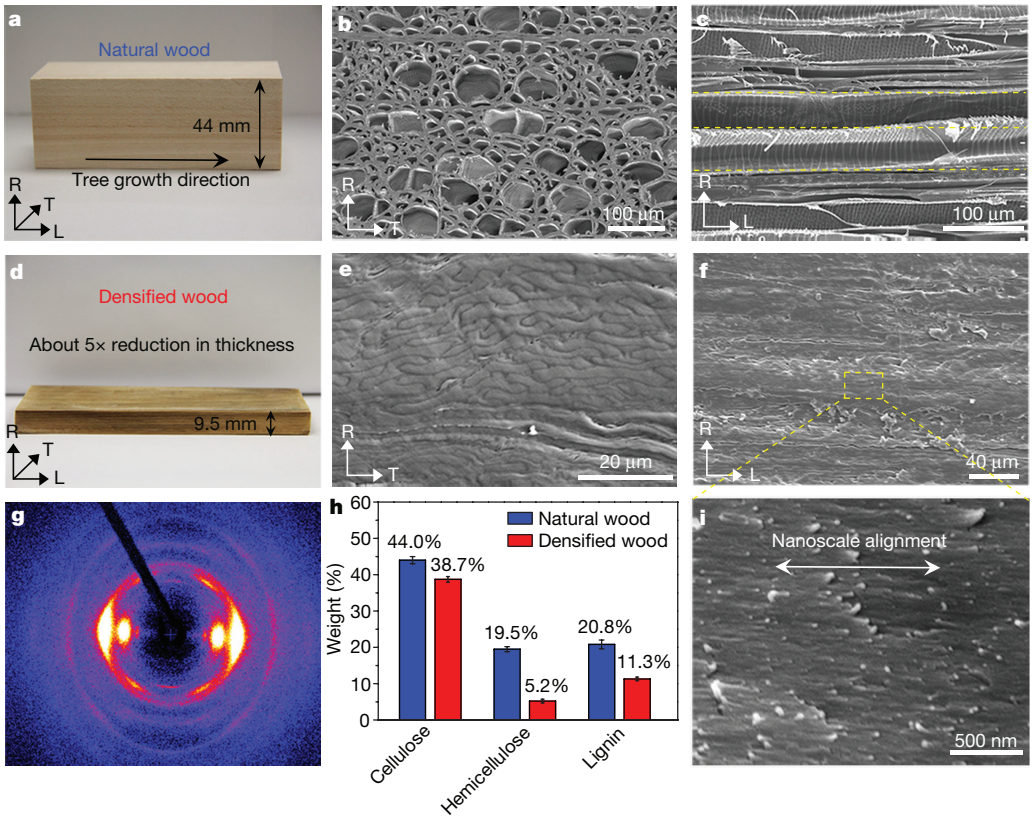

Figure 2 | Structural characterization of natural wood and densified wood. a, Photograph of natural wood sample. **b**, Scanning electron microscopy (SEM) image of the natural wood sample perpendicular to the tree growth (L) direction, clearly showing the porous structure in the RT plane. **c**, SEM image of the natural wood sample in the RL plane, revealing the cross-section view of the lumina along the L direction (highlighted by dashed lines). **d**, Photograph of densified wood. **e**, SEM image of the densified wood in the RT plane, showing the fully collapsed lumina. The open spaces between the cell walls in natural wood are eliminated, resulting in a unique laminated structure with cell walls tightly intertwined with each other. **f**, SEM image of the densified wood in the RL plane shows the dense laminated structure cross-section. **g**, Wide-angle X-ray diffraction pattern of the densified wood, showing that the cellulose nanofibre alignment is well preserved after densification. **h**, Chemical treatment leads to substantial removal of lignin (before, 20.8% ± 1.2%; after, 11.3% ± 0.5%) and hemicellulose (before, 19.5% ± 0.7%; after, 5.2% ± 0.5%) in natural wood, but only modest dissolution of cellulose content (before, 44.0% ± 1.0%; after, 38.7% ± 0.8%). **i**, Magnified SEM image of the densified wood, showing the highly aligned cellulose nanofibres.

Figure 1a shows a schematic of our top-down two-step approach to directly transforming bulk natural wood. Our approach involves partial removal of lignin/hemicellulose from bulk natural wood followed by hot-pressing (Fig. 1a; see Methods). Natural wood contains many lumina (tubular channels 20–80 μm in diameter) along the wood growth direction (Fig. 2a–c and Extended Data Fig. 1d, e). Chemical treatment leads to substantial reduction of lignin/hemicellulose content in natural wood, but only modest reduction of cellulose content, largely owing to the different stabilities of these three components in the $NaOH/Na_2SO_3$ solution (Fig. 2h). By partial removal of lignin/hemicellulose from the wood cell walls, the wood becomes more porous and less rigid (Extended Data Fig. 1a, b). Upon hot-pressing at 100 °C perpendicular to the wood growth direction, the wood lumina as well as the porous wood cell walls collapse entirely, resulting in a densified piece of wood reduced in thickness to about 20% (Fig. 2d) and with a threefold increase in density (Extended Data Fig. 1c). The densified wood has a unique microstructure: the fully collapsed wood cell walls are tightly intertwined along their cross-section (Fig. 2e and Extended Data Fig. 1g, j) and densely packed along their length direction (Fig. 2f and Extended Data Fig. 1h, i). By contrast, pure hot-pressing of natural wood without partial lignin/hemicellulose removal can only modestly densify the wood, leaving many gaps in between collapsed cell walls (Extended Data Fig. 2a–c). Wide-angle X-ray diffraction (Fig. 2g), small-angle X-ray scattering and scanning electron microscopy (SEM) (Fig. 2i and Extended Data Fig. 1k, l) further reveal that, at a finer scale, the cellulose nanofibres within the densified wood remain highly aligned, similar to natural wood but much more densely packed.

The mechanical properties of the densified wood are not only remarkably superior to those of natural wood, but also exceed those of many widely used structural materials (for example, plastics, steel and alloys). Figure 3a compares the tensile stress–strain curves for natural wood and densified wood. Both curves show a linear deformation behaviour before tensile failure. The densified wood demonstrates a record high tensile strength of 587 MPa, which is 11.5 times higher than that of the untreated natural wood (Fig. 3a, b), and also much higher than that of typical plastics[22–24] (such as nylon 6, polycarbonate, polystyrene and epoxy; Fig. 3c) and other densified woods (Extended Data Fig. 6m). A long-standing challenge in engineering material design is the conflict between strength and toughness, because these properties are in general mutually exclusive[25,26]. Interestingly, the large increase in tensile strength of the densified wood is not accompanied by a decrease in toughness. Both the work of fracture and the elastic stiffness of the densified wood are more than ten times higher than those of natural wood (Fig. 3b and Extended Data Fig. 3a). Charpy impact tests of the densified wood yield an impact toughness of 11.41 ± 0.5 J cm^{-2}, 8.3 times higher than that of the natural wood (1.38 ± 0.3 J cm^{-2}) (Extended Data Fig. 3d). The scratch hardness and hardness modulus of the densified wood are 30 times and 13 times higher than those of natural wood, respectively (Extended Data Fig. 3b, c, e). The flexural strength of the densified wood is about 6 times and 18 times higher than that of natural wood along and

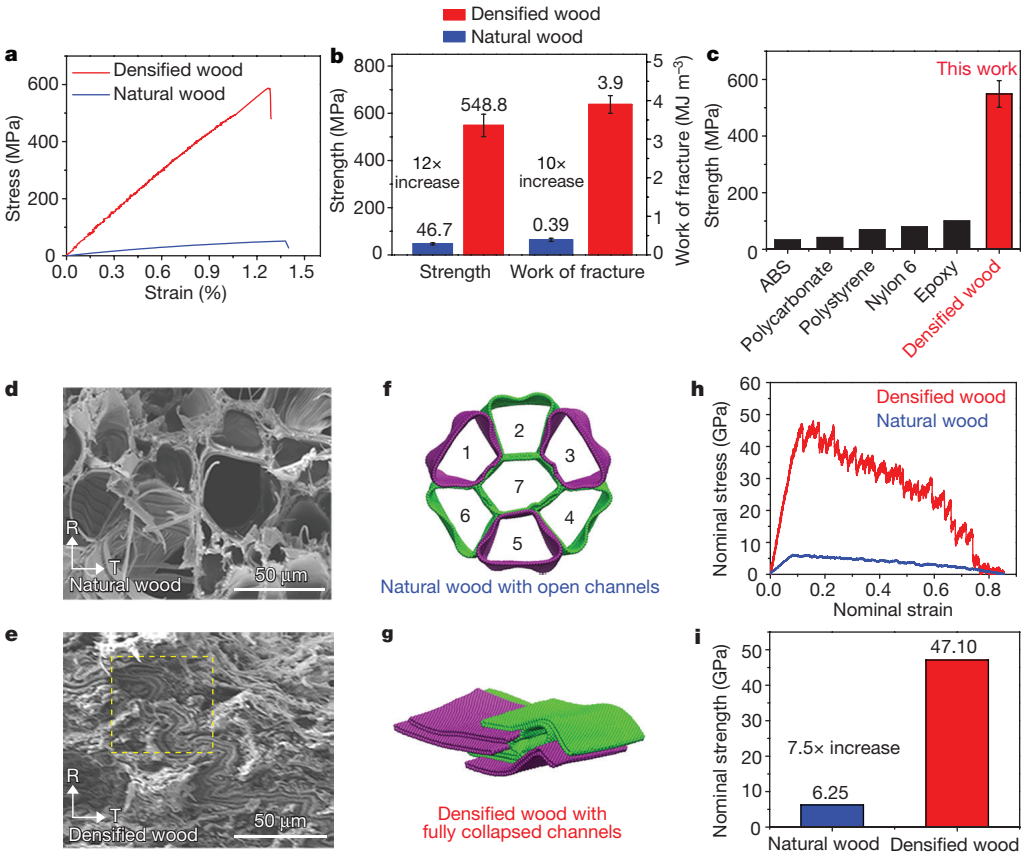

Figure 3 | Superb mechanical properties of densified wood and mechanistic understanding. a, Tensile stress–strain curves for natural wood and densified wood. **b**, Compared with natural wood (strength, 46.7 ± 4.5 MPa; work of fracture, 0.39 ± 0.04 MJ m^{-3}), the densified wood (strength, 548.8 ± 47.2 MPa; work of fracture, 3.9 ± 0.2 MJ m^{-3}) has greatly improved strength (12 times) and work of fracture (10 times). **c**, Comparison of the tensile strength of densified wood (548.8 ± 47.2 MPa) with other widely used polymer-based materials. **d**, **e**, SEM images of the tensile fracture surface of the natural wood and densified wood samples, respectively (RT plane). **f**, Simulation model of representative deformation and failure process in natural wood, containing a bundle of seven hollow wood lumina. **g**, Corresponding simulation model for densified wood with seven wood lumina fully collapsed. **h**, **i**, Simulated stress–strain curves for the relative sliding in the hollow lumina bundle and in collapsed lumina (**h**), which indicate a 7.5-fold increase in strength and work of fracture as a result of the densification treatment (**i**).

perpendicular to the growth direction, respectively (Extended Data Fig. 3f–n). The compressive strength of the densified wood is about 5.5 times and 33–52 times higher than that of natural wood along and perpendicular to the growth direction, respectively (Extended Data Fig. 4). We found that partial lignin removal allows for the highest density of the resulting wood with the best tensile strength, work of fracture and axial compressive strength (Extended Data Figs 2f–h and 4j). Without lignin removal, it is difficult to hot-press natural wood into a completely compact wood (Extended Data Fig. 2a–c shows numerous voids left between the cell walls). However, total lignin removal leads to wood that can be easily crushed during hot-pressing, probably owing to the absence of lignin as a binder (Extended Data Fig. 2d, e). The intrinsically light weight of cellulose also results in a specific strength of the densified wood (451 MPa cm^{-3} g^{-1}) even higher than that of lightweight titanium alloy (about 244 MPa cm^{-3} g^{-1}) (Fig. 1b)[27–30]. The densified wood is stable under moisture attack. For example, subjected to 95% relative humidity (RH) for 128 h, the densified wood swells to produce an increase of only 8.4% in thickness, with only a modest drop in tensile strength (493.1 ± 20.3 MPa, still 10.6 times higher than that of natural wood in ambient environment). Furthermore, by applying a standard surface treatment (painting), the densified wood is shown to be immune from moisture attack in the accelerated tests (Extended Data Fig. 5). More comprehensive studies demonstrate that our top-down two-step processing approach is universally effective for various species of wood (both hardwood and softwood) and can greatly enhance their strength and toughness simultaneously (Extended Data Fig. 6a–l).

A comparison between the tensile fracture surface of natural wood and that of the densified wood offers insights into the strengthening and toughening mechanisms in the densified wood. Tensile failure of natural wood initiates from relative sliding among open wood lumina followed by the pulling out and tearing of the wood lumina along the fracture surface (Fig. 3d and Extended Data Fig. 7a, b), while the tensile failure of the densified wood results from relative sliding among densely packed wood cell walls followed by the pulling out and fracture of the cell walls along the fracture surface (Fig. 3e and Extended Data Fig. 7c, d). Given that cellulose is the dominant constituent of the densified wood, the corresponding toughening and strengthening mechanisms can be understood as follows. The densely packed and intertwined wood cell walls in the densified wood at the microscale lead to a high degree of alignment of cellulose nanofibres and thus drastically increase the interfacial area among nanofibres. At the molecular scale, owing to the rich hydroxyl groups in cellulose molecular chains, relative sliding among densely packed wood cell walls involves an enormous number of repeating events of hydrogen-bond formation, breaking and reformation at the molecular scale[8] (Fig. 1a and Extended Data Fig. 1m). Consequently, the total energy needed to fracture the densified wood is much higher than that needed to fracture natural wood. In other words, the densified wood is much tougher than natural wood. The densely packed microstructure also greatly reduces both the quantity and size of defects (ranging from vessels to tracheids and pits on cell walls; Extended Data Fig. 1d–i) in the densified wood, producing a much higher strength than that of natural wood. Further modelling of the mechanics of the envisioned deformation and failure processes

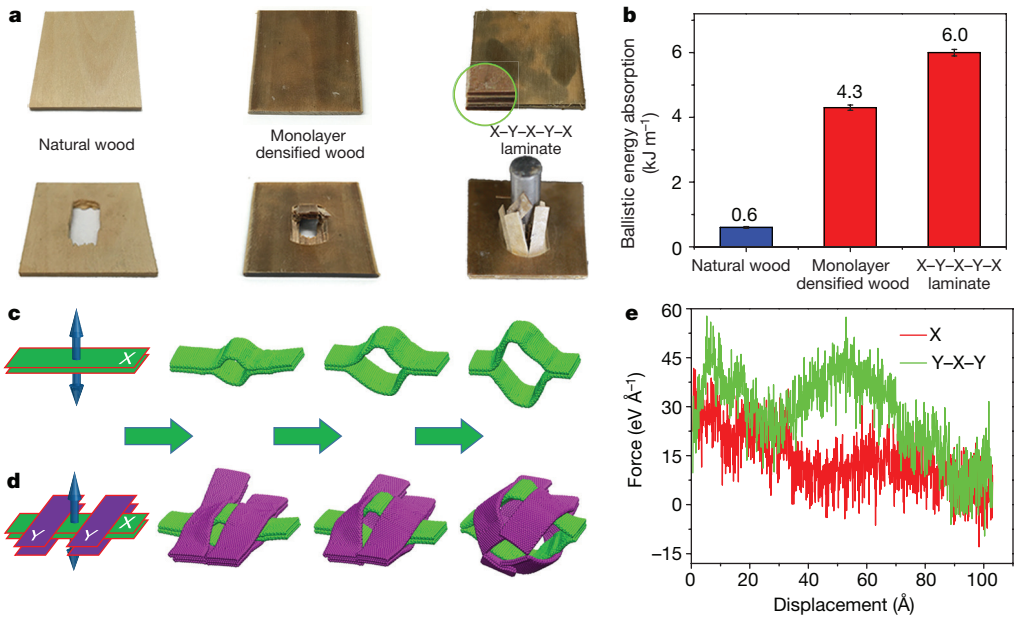

Figure 4 | Ballistic test. a, Photographs of the natural wood, monolayer densified wood and the X–Y–X–Y–X laminated densified wood before (top row) and after (bottom row) the ballistic test. **b**, Comparison of ballistic energy absorption of three types of wood (natural wood, 0.60 ± 0.03 kJ m^{-1}; monolayer densified wood, 4.30 ± 0.08 kJ m^{-1}; X–Y–X–Y–X laminate, 6.0 ± 0.1 kJ m^{-1}). **c**, **d**, Mechanistic understanding of enhanced ballistic resistance in laminated densified wood. Simulation trajectory snapshots during the separation of two neighbouring collapsed wood cell walls in parallel are shown (**c**) along with simulation snapshots for the same two wood cell walls sandwiched between another two pairs of collapsed wood cell walls along the perpendicular direction at different separation displacements (**d**). **e**, The separation force as a function of separation displacement. The area below the curve indicates energy dissipation. The sandwiched configuration (corresponding to laminated densified wood) could dissipate more energy than the parallel configuration (corresponding to monolayer densified wood).

in natural wood and densified wood (details in Methods) quantitatively verifies the above strengthening and toughening mechanisms. It is shown that both the maximum nominal stress (indicating strength) and the energy dissipation (indicating toughness) associated with sliding between the densely packed collapsed wood lumina are about 7.5 times higher than those associated with hollow wood lumina (Fig. 3f–i and Extended Data Fig. 8a–c). Hydrogen bonds formed between neighbouring cellulose nanofibres make a pivotal contribution to the remarkably enhanced strength and toughness (Extended Data Fig. 8d–f).

The well-aligned cellulose nanofibres dictate the anisotropic mechanical properties of densified wood (Extended Data Fig. 9a–c). To explore the full potential of the exceptional mechanical properties of densified wood, we laminated two layers of natural wood with perpendicular wood fibre orientations, and followed the same processing process to obtain a bilayer densified wood (referred to as X–Y). Tensile strengths of the X–Y densified wood along two perpendicular wood fibre directions are shown to be nearly the same (221.6 ± 20.0 MPa and 225.6 ± 18.0 MPa, respectively, Extended Data Fig. 9d–f), and much higher than the T-direction strength of monolayer densified wood (43.3 ± 2.0 MPa) or that of natural wood (5.1 ± 0.4 MPa).

These strong and tough yet lightweight densified woods hold promise as materials for low-cost armour and ballistic energy absorption. To demonstrate such a potential, we used the same processing approach to make a five-layer densified wood with fibre orientation alternating by 90° from layer to layer (referred to as X–Y–X–Y–X). We performed ballistic tests (see Methods) on natural wood, monolayer densified wood and X–Y–X–Y–X densified wood in an air-gun ballistic tester (Extended Data Fig. 10a and Fig. 4a). The ballistic energy absorption per unit sample thickness for monolayer densified wood is 4.3 ± 0.08 kJ m^{-1}, a remarkable sevenfold increase from that of natural wood (0.6 ± 0.03 kJ m^{-1}). High-speed-camera videos of the ballistic tests (see Supplementary Video 1) and further characterization of the fractured samples (Extended Data Fig. 10b–g) reveal that in the monolayer densified wood, the perforation opening by the steel projectile is smaller than that in the natural wood, and the wood surface is severely chapped, indicating much stronger bonding between highly packed wood cell walls (Fig. 4a). The ballistic resistance of the X–Y–X–Y–X densified wood is shown to be even higher and also more isotropic (Extended Data Fig. 10h). The projectile can break through the sample surface but is eventually trapped inside the sample without complete perforation. The resulting ballistic energy absorption is 6.0 ± 0.1 kJ m^{-1}, ten times higher than that of natural wood (Fig. 4b). Further mechanics modelling attributes this enhanced and isotropic ballistic resistance to the reinforcement effect acting between the neighbouring wood layers of alternating orientation (Fig. 4c–e and Extended Data Fig. 10i–l).

Online Content Methods, along with any additional Extended Data display items and Source Data, are available in the online version of the paper; references unique to these sections appear only in the online paper.

Received 14 May; accepted 8 December 2017.

1. Wang, J., Cheng, Q. & Tang, Z. Layered nanocomposites inspired by the structure and mechanical properties of nacre. *Chem. Soc. Rev.* **41,** 1111–1129 (2012).
2. Militzer, M. A synchrotron look at steel. *Science* **298,** 975–976 (2002).
3. Podsiadlo, P. *et al.* Ultrastrong and stiff layered polymer nanocomposites. *Science* **318,** 80–83 (2007).
4. Zhu, Y. T. & Liao, X. Nanostructured metals: retaining ductility. *Nat. Mater.* **3,** 351–352 (2004).
5. Fratzl, P. & Weinkamer, R. Nature's hierarchical materials. *Prog. Mater. Sci.* **52,** 1263–1334 (2007).
6. Gao, H., Ji, B., Jäger, I. L., Arzt, E. & Fratzl, P. Materials become insensitive to flaws at nanoscale: lessons from nature. *Proc. Natl Acad. Sci. USA* **100,** 5597–5600 (2003).
7. Meyers, M. A., McKittrick, J. & Chen, P.-Y. Structural biological materials: critical mechanics-materials connections. *Science* **339,** 773–779 (2013).
8. Zhu, H. *et al.* Anomalous scaling law of strength and toughness of cellulose nanopaper. *Proc. Natl Acad. Sci. USA* **112,** 8971–8976 (2015).
9. Hon, D. N.-S. & Shiraishi, N. *Wood and Cellulosic Chemistry* (CRC Press, 2000).
10. Erickson, E. *Mechanical Properties of Laminated Modified Wood* (US Department of Agriculture, Forest Service, Forest Products Laboratory, 1965).
11. Fang, C.-H., Mariotti, N., Cloutier, A., Koubaa, A. & Blanchet, P. Densification of wood veneers by compression combined with heat and steam. *Eur. J. Wood Wood Prod.* **70,** 155–163 (2012).

12. Bekhta, P., Hiziroglu, S. & Shepelyuk, O. Properties of plywood manufactured from compressed veneer as building material. *Mater. Des.* **30,** 947–953 (2009).
13. Kultikova, E. V. *Structure and Properties Relationships of Densified Wood* (Virginia Polytechnic Institute and State University, 1999).
14. Pařil, P. *et al.* Comparison of selected physical and mechanical properties of densified beech wood plasticized by ammonia and saturated steam. *Eur. J. Wood Wood Prod.* **72,** 583–591 (2014).
15. Navi, P. & Heger, F. Combined densification and thermo-hydro-mechanical processing of wood. *MRS Bull.* **29,** 332–336 (2004).
16. Gong, M., Lamason, C. & Li, L. Interactive effect of surface densification and post-heat-treatment on aspen wood. *J. Mater. Process. Technol.* **210,** 293–296 (2010).
17. O'Connor, J. P. *Improving wood strength and stiffness through viscoelastic thermal compression*. Masters thesis, Oregon State Univ., https://ir.library.oregonstate.edu/concern/graduate_thesis_or_dissertations/8623j074v (2007).
18. Laine, K., Segerholm, K., Wålinder, M., Rautkari, L. & Hughes, M. Wood densification and thermal modification: hardness, set-recovery and micromorphology. *Wood Sci. Technol.* **50,** 883–894 (2016).
19. Kutnar, A. & Kamke, F. A. Compression of wood under saturated steam, superheated steam, and transient conditions at 150 °C, 160 °C, and 170 °C. *Wood Sci. Technol.* **46,** 73–88 (2012).
20. Hill, C. A. *et al.* The water vapour sorption properties of thermally modified and densified wood. *J. Mater. Sci.* **47,** 3191–3197 (2012).
21. Laine, K. *et al.* Measuring the thickness swelling and set-recovery of densified and thermally modified Scots pine solid wood. *J. Mater. Sci.* **48,** 8530–8538 (2013).
22. Li, Y. & Shimizu, H. Improvement in toughness of poly(L-lactide) (PLLA) through reactive blending with acrylonitrile–butadiene–styrene copolymer (ABS): morphology and properties. *Eur. Polym. J.* **45,** 738–746 (2009).
23. Kim, K. H. & Jo, W. H. A strategy for enhancement of mechanical and electrical properties of polycarbonate/multi-walled carbon nanotube composites. *Carbon* **47,** 1126–1134 (2009).
24. Ku, H., Wang, H., Pattarachaiyakoop, N. & Trada, M. A review on the tensile properties of natural fiber reinforced polymer composites. *Composites B* **42,** 856–873 (2011).
25. Ritchie, R. O. The conflicts between strength and toughness. *Nat. Mater.* **10,** 817–822 (2011).
26. Wang, Y., Chen, M., Zhou, F. & Ma, E. High tensile ductility in a nanostructured metal. *Nature* **419,** 912–915 (2002).
27. Dursun, T. & Soutis, C. Recent developments in advanced aircraft aluminium alloys. *Mater. Des.* **56,** 862–871 (2014).
28. Frommeyer, G. & Brüx, U. Microstructures and mechanical properties of high-strength Fe-Mn-Al-C light-weight TRIPLEX steels. *Steel Res. Int.* **77,** 627–633 (2006).
29. Gil, F., Manero, J., Ginebra, M. & Planell, J. The effect of cooling rate on the cyclic deformation of beta-annealed Ti-6Al-4V. *Mater. Sci. Eng. A* **349,** 150–155 (2003).
30. Kim, S.-H., Kim, H. & Kim, N. J. Brittle intermetallic compound makes ultrastrong low-density steel with large ductility. *Nature* **518,** 77–79 (2015).

Supplementary Information is available in the online version of the paper.

Acknowledgements We thank R. Briber for suggestions and R. J. Bonenberger for help with mechanical tests. We acknowledge the support of the Maryland NanoCenter and its AIMLab. J.S. acknowledges financial support from the China Scholarship Council.

Author Contributions J.S., C.C., S.Z. and M.Z. contributed equally to this work. L.H., J.S., C.C. and M.Z. contributed to the initiating idea. J.S. and C.C. contributed to the wood densification and mechanical measurements. Yo.L., U.R., Z.J., N.Q., U.H.L., H.A.B. and T.L. contributed to the mechanical tensile and ballistic tests. J.D. and Y.K. contributed to the 3D illustrations. Yi.L., C.C., Y.Y. and A.G. contributed to characterization via SEM. J.Y.Z. performed the compositional analysis. A.V. and A.M. contributed to the indentation and scratch hardness tests. S.Z. and T.L. contributed to both mechanical simulations and analysis. H.L. and M.L.M. contributed to XRD measurement and analysis. T.L., L.H., J.S. and C.C. contributed to the writing of the paper. All authors contributed to commenting on the final manuscript.

Author Information Reprints and permissions information is available at www.nature.com/reprints. The authors declare no competing financial interests. Readers are welcome to comment on the online version of the paper. Publisher's note: Springer Nature remains neutral with regard to jurisdictional claims in published maps and institutional affiliations. Correspondence and requests for materials should be addressed to L.H. (binghu@umd.edu) or T.L. (lit@umd.edu).

Reviewer Information *Nature* thanks A. Cloutier, S. Eichhorn and the other anonymous reviewer(s) for their contribution to the peer review of this work.

METHODS

Materials and chemicals. Basswood (*Tilia*), oak (*Quercus*), poplar (*Populus*), western red cedar (*Thuja plicata*) and eastern white pine (*Pinus strobus*) were used for the fabrication of densified wood. Sodium hydroxide (>97%, Sigma-Aldrich) and sodium sulfite (>98%, Sigma-Aldrich) and deionized (DI) water were used for processing the wood.

Two-step process towards densified wood. First, natural wood blocks (typical sample dimension: 120.0 mm by 44.0 mm by 44.0 mm) were immersed in a boiling aqueous solution of mixed 2.5 M NaOH and 0.4 M Na_2SO_3 for 7 h, followed by immersion in boiling deionized water several times to remove the chemicals. Next, the wood blocks were pressed at 100 °C under a pressure of about 5 MPa for about 1 day to obtain the densified wood (115.6 mm by 46.5 mm by 9.5 mm). By adjusting the boiling times, densified wood with different degrees of lignin removal can be obtained.

Mechanical tests. The tensile, bending and compressive properties of the wood samples were measured using a Tinius Olsen H5KT tester. The dimensions for tensile samples were approximately 100 mm by 6 mm by 1.5 mm. The samples were clamped at both ends and stretched along the sample length direction until they fractured with a constant test speed of 5 mm min^{-1} at room temperature. The dimensions for bending samples were approximately 35 mm by 5 mm by 4 mm. Three-point bending tests were conducted for these samples, with the span between the two bottom rollers 20 mm and the top roller pressing down at the centre at a speed of 1 mm min^{-1}. The flexural stress is defined as the maximum tensile stress at the bottom surface of the sample right below the top roller. The dimensions for compressive samples were approximately 9 mm long, 9 mm wide and 4.5 mm thick, and the samples were compressed along the thickness direction at a speed of 1 mm min^{-1}.

Scratch hardness test. The scratch resistance of wood samples was evaluated according to the Standard Test Method for Scratch Hardness, ASTM G171-03(2009) using a linear reciprocating tribometer (Rtec Instruments Multi-Function Tribometer). The test was performed by applying a normal load on a diamond sphero-conical tip indenter and moving the wood surface laterally relative to the indenter at a constant speed. The width of the scratch was then measured using an optical microscope and the scratch hardness number (in gigapascals) was calculated as kP/w^2, where P is the applied normal force, w is the scratch width and k is the geometric constant. Each scratch hardness value was determined as an arithmetic mean of a set of three scratches made side by side at different locations. The lateral speed of the sample and the stroke length of the scratch were chosen as 0.2 mm s^{-1} and 7 mm, respectively.

Hardness modulus test. The hardness modulus was measured using a modified version of the standard procedure described in the ASTM D1037-121 with an Rtec Instruments Multi-Function Tribometer. The standard recommends indenting specimens of thickness 3–6 mm, using a ball of diameter 1.3 mm, to a depth of 2.5 mm. Since our test specimens are 5 mm thick, we used a smaller ball of diameter 4.76 mm with a penetration depth of 1.05 mm, which corresponds to an average Hertzian contact pressure equal to that in the standard test. The rate of penetration was constant at the recommended value of 1.3 mm min^{-1}. The penetration force versus depth was plotted and the slope of the linear portion of this curve was calculated as the hardness modulus (pounds per inch). Five indentations were made on each specimen and the average value was reported.

Charpy impact test. The Charpy impact test of the wood samples was performed on a Tinius Olsen pendulum impact tester. The dimensions of the samples were 14 mm × 4.5 mm × 100 mm.

Ballistic test. We performed the ballistic tests on wood samples using a gas gun, which comprises a pressure indicator frame, two cylinders filled with compressed nitrogen (N_2), a pressure chamber 127 mm in diameter and barrel-length 190.5 mm, a nozzle of length 1,156 mm and internal diameter 12.5 mm and a holder specifically designed to clamp the sample. The pressure indicator frame has dials with which we adjusted the pressure inside the two N_2 cylinders. The left cylinder is used to pressurize the volume inside the barrel chamber when the projectile is fired and the right N_2 cylinder controls the pressure for the firing valve, helping it open instantaneously when fired. The chamber pressure was set to about 2.22 MPa. Once opened, the valve releases the pressure and accelerates the projectile. We used projectiles cylindrical in shape, made of stainless steel, with a diameter of 11.85 mm, length 51.77 mm and mass 0.046 kg. The dimensions of the samples were approximately 44 mm by 44 mm by 3 mm. The whole ballistic process was captured using two Phantom v12 cameras. The Phantom Camera Control software (http://www.phantomhighspeed.com/products/accessories-and-options/camera-control-software), developed for such high-speed digital cameras, captured the velocities of the projectile before and after perforating the sample. The ballistic energy absorption of the test sample is defined by the kinetic energy loss after a cylindrical steel projectile perforates the sample. The equation for the ballistic energy absorption normalized by sample thickness is $m(v_1^2 - v_2^2)/2t$, where m is the mass of the projectile, t is the thickness of the sample and v_1 and v_2 are the velocities of the projectile before and after perforating the sample, respectively.

Accelerated test against moisture. The humidity chamber (LHS-150HC-II) was set up at 20 °C, 95% RH. Then pre-cut samples with dimensions of approximately 15 mm by 15 mm by 4.6 mm were placed in the humidity chamber. The dimensions and weight of the samples after various intervals in the humidity chamber were recorded. Following a painting method widely used in the wood industry, we coated the densified wood with a thin layer of oil-based paint (Polyurethane, Minwax). After the paint was totally dry, the sample was put into the humidity chamber and measured at regular intervals.

Characterizations. A scanning electron microscope (SEM, Hitachi SU-70) was used to characterize the morphologies of the wood samples. Small-angle X-ray scattering (SAXS) patterns for three samples of each wood were collected using Rigaku MicroMax 007HF (operating voltage at 40 kV, current at 30 mA, CuKα, $\lambda = 0.1541$ nm). The angle between the incident X-ray beam and the width direction on the sample was kept at 90°. The raw azimuthal intensity distribution was extracted and the baseline is subtracted. Wide-angle X-ray diffraction patterns were collected on multi-filament bundles using a Rigaku RAPID II (operating voltage at 40 kV, current at 30 mA, CuKα, $\lambda = 0.1541$ nm) equipped with a curved detector manufactured by Rigaku Americas Corporation. Compositional analysis of natural wood and chemical-treated wood was carried out on a high-performance liquid chromatography (HPLC) system (Ultimate 3000, Thermo Scientific, USA).

Mechanics modelling. We used a generic coarse-grained simulation scheme to qualitatively reveal the underlying mechanism for the enhancement in mechanical properties. The wood fibre is modelled as a tube made of coarse-grained beads that assume a hexagonal lattice structure (Extended Data Fig. 8d). The bonded energy terms of the coarse-grained scheme consist of a two-body bond energy and three-body angle energy and a four-body torsion energy as follows:

$$U_{\text{bonded}}(r_{ij}, \theta_{ijk}) = \sum \frac{1}{2} K_{\text{bond}} (r_{ij} - r_0)^2 + \sum \frac{1}{2} K_\theta (\cos\theta_{ijk} - \cos\theta_0)^2 + \sum_{n=1,5} A_n \cos^{n-1}\Phi$$

where K_{bond} and K_θ are the bond force constant and the angle force constant, respectively, r_{ij} is the distance between the ith and jth coarse-grained beads while r_0 is the corresponding equilibrium value of r_{ij}; θ_{ijk} is the angle formed between the i–j bond and the j–k bond while θ_0 is the corresponding equilibrium value of θ_{ijk} (which is 120° for all cases). A_n are coefficients ($n = 1, 2, 3, 4, 5$) for the dihedral angle Φ. The non-bonded term includes the long-range van der Waals Lennard–Jones-type interaction $4\varepsilon[(\sigma/r)^{12} - (\sigma/r)^6]$ between coarse-grained beads (cut-off distance 1 nm, ε denotes the interaction strength and σ denotes the distance where the interaction energy crosses zero) and a short-range (cut-off distance 0.24 nm) Morse-type potential $D_0[e^{-2\alpha(r - r_{\text{Morse }0})} - 2e^{-\alpha(r - r_{\text{Morse }0})}]$, which is used to model the hydrogen-bond interaction among wood fibres. The simulation is done at 300 K by canonical ensemble and by Nose–Hoover thermostat. Extended Data Fig. 8g lists the values of the coarse-grained parameters used in the simulations.

Data availability. The data that support the findings of this study are available from the corresponding authors on reasonable request.

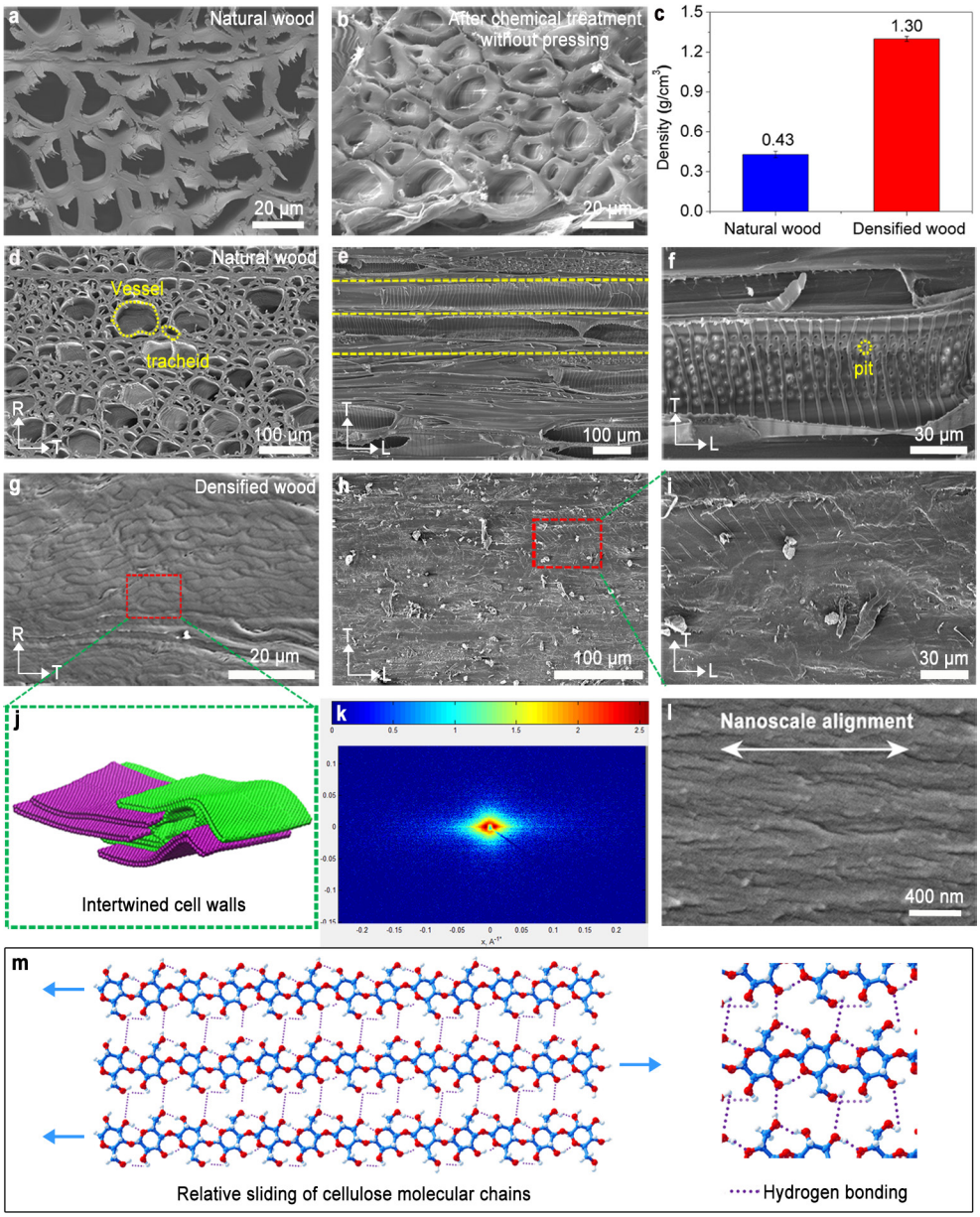

Extended Data Figure 1 | Structural characterization of natural wood and densified wood. a, **b**, Comparison of SEM images of natural wood (**a**) and the wood after partial lignin removal but without lateral hot-pressing (**b**) shows that lignin between the cell walls is partially removed. **c**, Comparison of densities of natural (0.43 ± 0.02 g cm^{-3}) and densified woods (1.30 ± 0.02 g cm^{-3}). **d**–**f**, SEM images of the cross-section of natural wood in the RT (**d**) and TL (**e**, **f**) planes show intrinsic defects such as vessels and tracheids along the L direction and pits in the cell walls. **g**–**j**, The corresponding SEM images of densified wood show that the hollow lumina are completely collapsed to form highly intertwined wood cell walls (**g**), as verified by the simulation model (**j**), and even the tiny pits in the wood cell walls are eliminated owing to the densification (**h**, **i**). **k**–**m**, The small-angle X-ray scattering pattern (**k**) and the high-magnification SEM image (**l**) show well-aligned cellulose nanofibres in densified wood, which greatly facilitate the formation of hydrogen bonds in neighbouring cellulose molecular chains during their relative sliding (**m**).

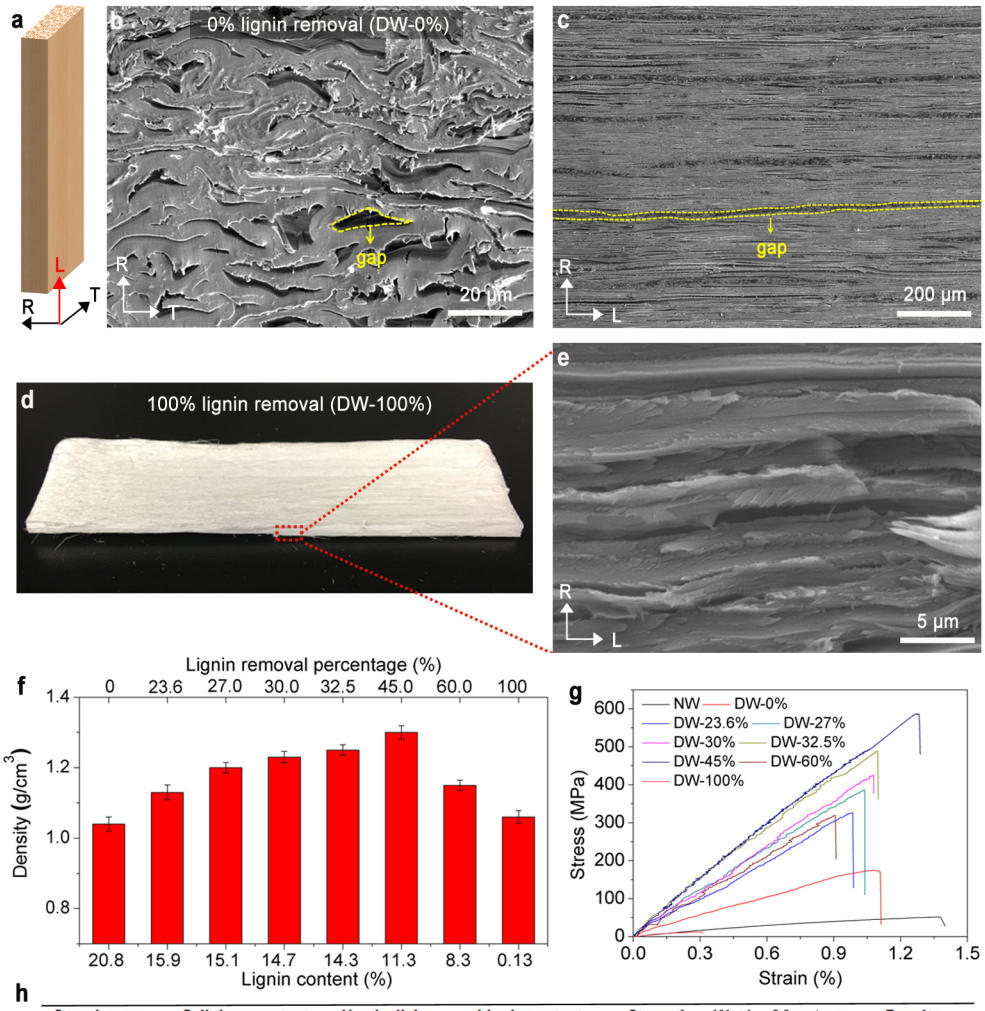

h

Sample name	Cellulose content (%)	Hemicellulose content (%)	Lignin content (%)	Strength (MPa)	Work of fracture (MJ/m³)	Density (g/cm³)
NW	44.01	19.5	20.8	51.6	0.43	0.46
DW-0%	44.01	19.5	20.8	175.0	1.1	1.04
DW-23.6%	42.2	10.6	15.9	325.6	1.6	1.13
DW-27%	40.2	9.2	15.1	386.3	2.1	1.20
DW-30%	38.2	7.2	14.7	425.6	2.3	1.23
DW-32.5%	38.1	6.8	14.3	488.8	2.9	1.25
DW-45%	**38.7**	**5.2**	**11.3**	**586.8**	**4.0**	**1.3**
DW-60%	35.4	3.8	8.2	319.0	1.48	1.15
DW-100%	31.2	1.89	0.13	12.5	0.02	1.06

Extended Data Figure 2 | Effect of degree of lignin removal on wood structure and mechanical properties. a, Schematics of wood sample with the L direction as the tree-growth direction. **b**, **c**, SEM images of the cross-sections in the RT plane (**b**) and the RL plane (**c**) of a pressed wood sample with 0% lignin removal, which show a large number of gaps remaining in between partially collapsed cell walls. **d**, **e**, Photo and SEM image of the densified wood with 100% lignin removal show that the pressed cell walls are separated from each other owing to the absence of lignin as binding agent. **f**, **g**, Densities (**f**) and tensile stress–strain curves (**g**) of densified woods with various degrees of lignin removal. **h**, Summary of cellulose/hemicellulose/lignin contents as well as strength, work of fracture and density under various degrees of lignin removal. Densified wood with 45% lignin removal is shown to have the highest strength, work of fracture and density. DW-*x* refers to densified wood with a certain amount (*x*) of lignin removal and subsequent densification, whereas NW refers to natural wood without lignin removal or densification.

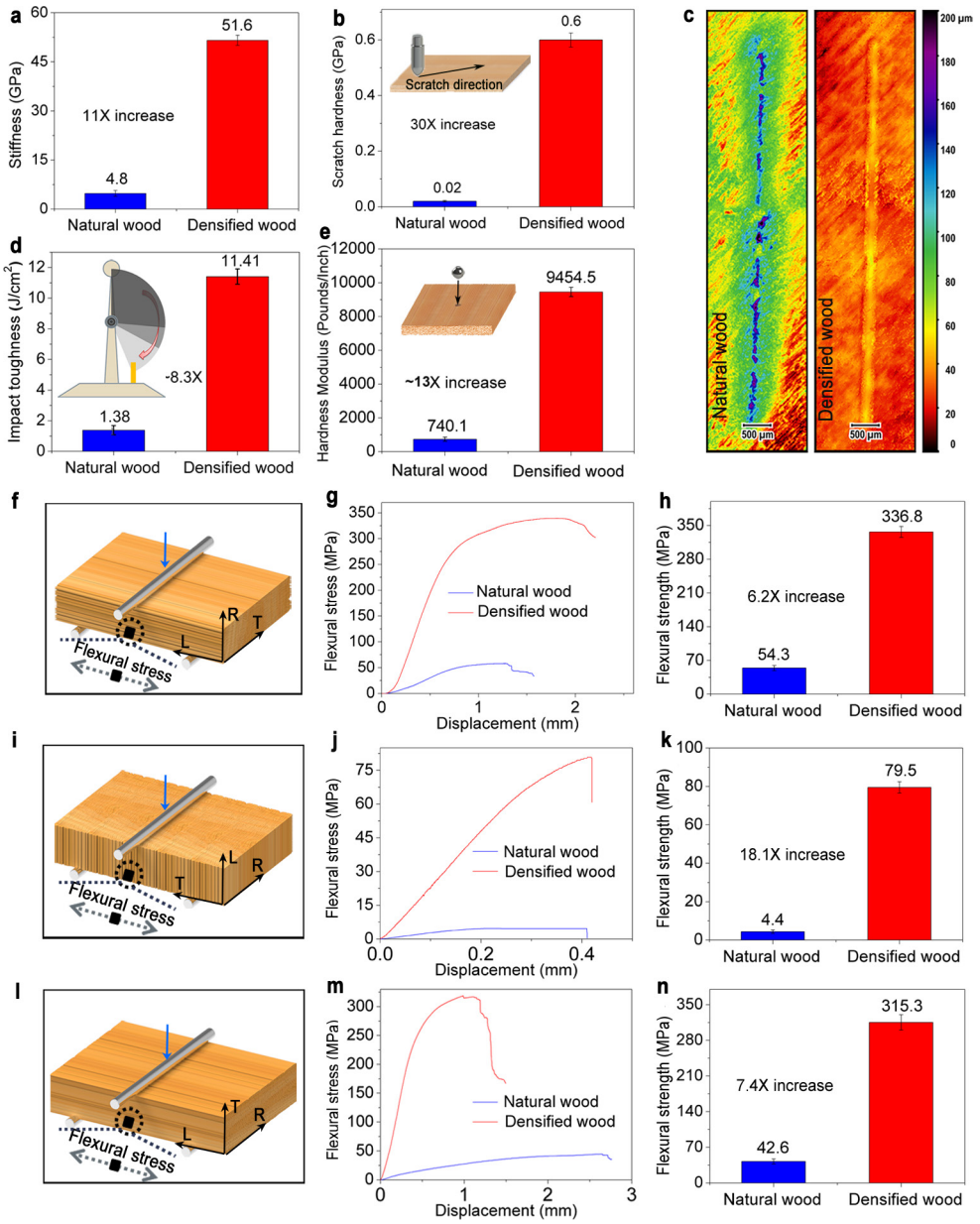

Extended Data Figure 3 | Comparison of mechanical properties of natural wood and densified wood. a, Stiffness (natural wood, 4.8 ± 0.9 GPa; densified wood, 51.6 ± 1.5 GPa). **b**, Scratch hardness (natural wood, 0.02 ± 0.0029 GPa; densified wood, 0.6 ± 0.025 GPa). **c**, Interferometer images of scratches on natural wood and densified wood, showing the notable decrease of the scratch depth of the densified wood owing to increased hardness. **d**, Charpy impact toughness (densified wood, 11.41 ± 0.5 J cm^{-2}; natural wood, 1.38 ± 0.3 J cm^{-2}). **e**, Hardness modulus (natural wood, 740.1 ± 115.4 pounds per inch; densified wood, 9454.5 ± 273.3 pounds per inch). **f**, **i**, **l**, Schematics of bending tests along three different directions. **g**, **j**, **m**, Corresponding flexural stress as a function of roller displacement (bending deflection) for natural wood and densified wood. **h**, **k**, **n**, Comparison of the corresponding flexural strengths of natural wood (with the roller along the T direction, 54.3 ± 5.1 MPa; perpendicular to wood growth direction, 4.4 ± 0.9 MPa; with the roller along the R direction, 42.6 ± 4.9 MPa; eight samples tested for each direction) and densified wood (with the roller along the T direction, 336.8 ± 11.3 MPa; perpendicular to wood growth direction, 79.5 ± 3.0 MPa; with the roller along the R direction, 315.3 ± 14.8 MPa; eight samples tested for each direction).

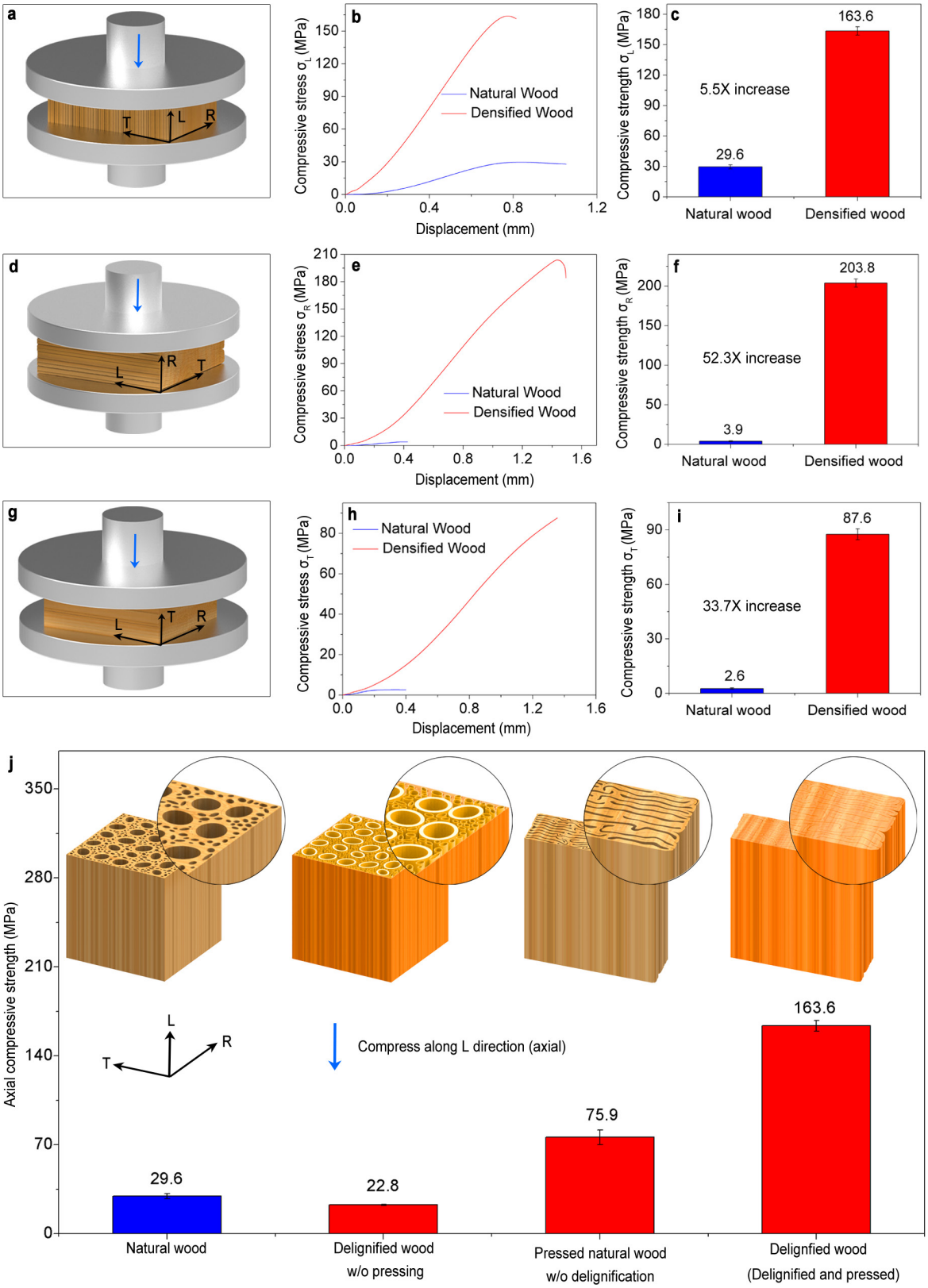

Extended Data Figure 4 | Compressive strength of natural wood and densified wood. a, **d**, **g**, Schematics of compression tests along three different directions. **b**, **e**, **h**, Corresponding compressive stress as a function of compressive displacement for natural wood and densified wood. **c**, **f**, **i**, Comparison of the corresponding compressive strengths of natural wood (L direction, 29.6 ± 2.0 MPa; R direction, 3.9 ± 0.6 MPa; T direction, 2.6 ± 0.4 MPa; eight samples tested for each direction) and densified wood (L direction, 163.6 ± 4.1 MPa; R direction, 203.8 ± 5.2 MPa; T direction, 87.6 ± 3.0 MPa; eight samples tested for each direction). **j**, Comparison of axial compressive strengths (along the L direction) of natural wood, delignified wood without hot-pressing, pressed natural wood without delignification, and densified wood (delignified and then hot-pressed). Insets illustrate the representative cross-section features of the four types of wood.

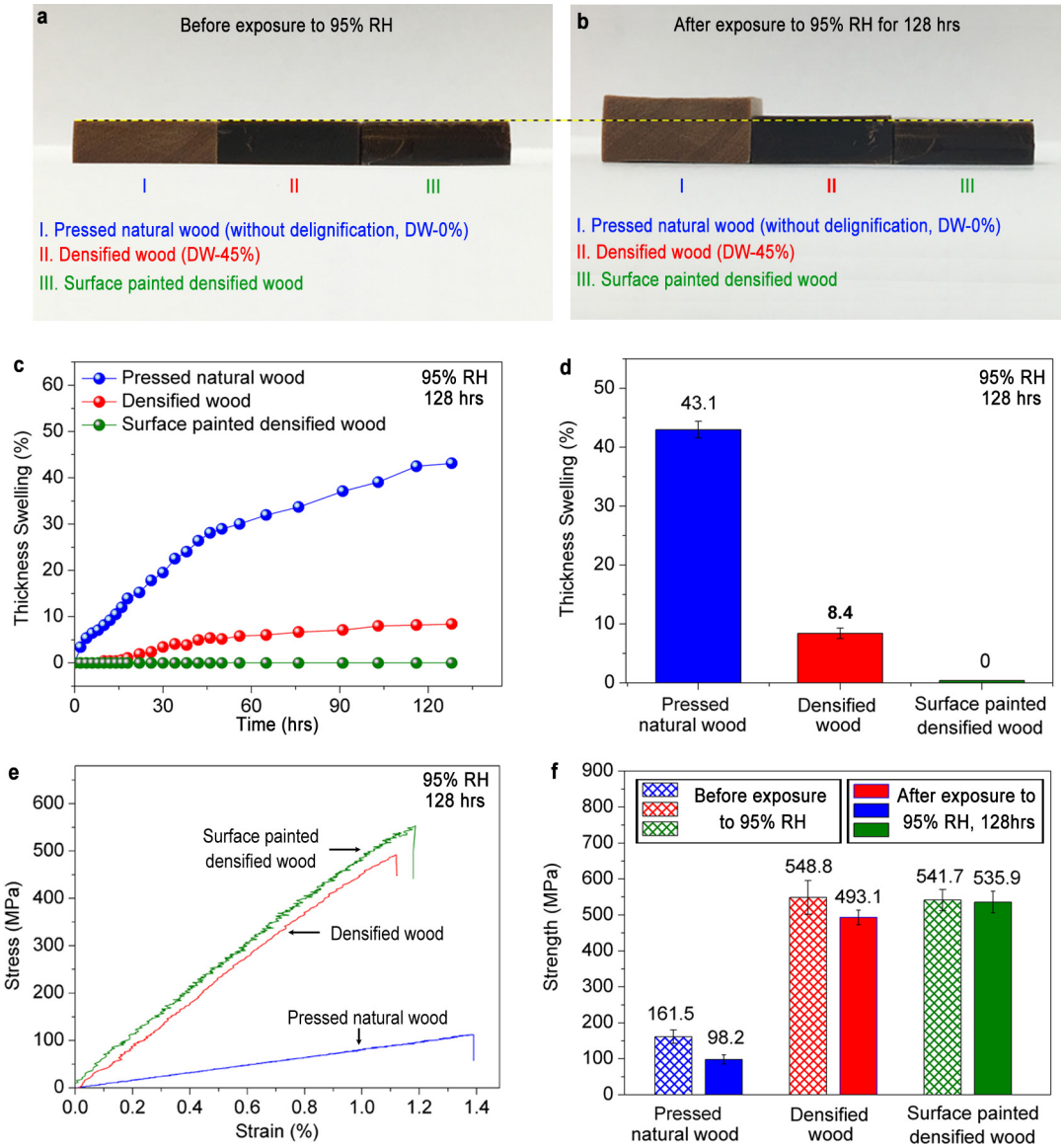

Extended Data Figure 5 | Dimensional stability and mechanical properties of pressed natural wood, densified wood and surface-painted densified wood against moisture. a, **b**, Photographs of pressed natural wood without delignification, densified wood (45% lignin removal and then hot-pressed) and surface-painted densified wood before (**a**) and after (**b**) sustaining 95% RH for 128 h. **c**, Change in thickness of the three wood samples over time. **d**, Percentage increase in thickness (pressed natural wood, 43.1% ± 1.4%; densified wood, 8.4% ± 0.9%; surface-painted densified wood, 0%). **e**, Tensile stress–strain curves of the three wood samples after sustaining 95% RH for 128 h. **f**, Strengths of the three wood samples before (pressed natural wood, 161.5 ± 18.8 MPa; densified wood, 548.8 ± 47.2 MPa; surface-painted densified wood, 541.7 ± 29.2 MPa) and after (pressed natural wood, 98.2 ± 12.6 MPa; densified wood, 493.1 ± 20.3 MPa; surface-painted densified wood, 535.9 ± 30.0 MPa) sustaining 95% RH for 128 h.

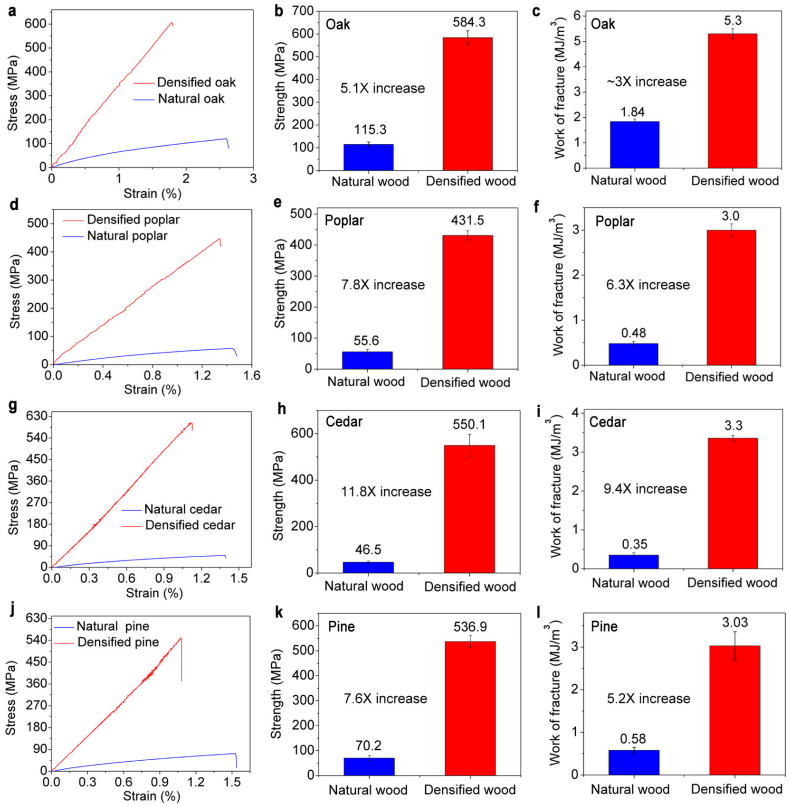

m

Treatment	Lignin Removal	Wood materials	Ultimate tensile strength (MPa)			Compression ratio (%)	Structure	Ref.
			Before pressing	After pressing	Enhancement			
Compressed at ~180 °C and 65% relative humidity	No	Sitka spruce	~88	~320	~3.6	~60	Densified	Ref. 10
	No	Sweetgum	~102	~220	~2.2	~55	Densified	
	No	Yellow birch	~151	~307	~2	~47	Densified	
Fill in resin and compress	No	Sitka spruce	~88	~166	~1.9	<50	Densified	Ref. 10
	No	Sweetgum	~102	~185	~1.8	<50	Densified	
	No	Yellow birch	~151	~210	~1.4	<50	Densified	
Combined with heat (160°C), steam (550 KPa), and pressure.	No	Aspen	~60	~120	2	~50	Densified	Ref. 11
Cold rolling process	No	Birch	128.2	130-164	1.3	5-25	Densified	Ref. 12
	No	Alder	63.5	64-113.6	1.8	5-25	Densified	
90 °C, 95% relative humidity, 93 KPa	No	Loblolly pine	117	204	1.7	50	Densified	Ref. 13
	No	Yellow poplar	121	197	1.6	50	Densified	
Ammonia and saturated steam	No	Beech	—	—	—	15, 30, 50	Densified with pores	Ref. 14
Steam & press	No	Spruce	—	—	—	~60	Densified with pores	Ref. 15
Densification & post-heat-treatment	No	Aspen	—	—	—	50	Densified with pores	Ref. 16
Viscoelastic Thermal Compression	No	Eastern cottonwood	—	—	—	~50	Densified with pores	Ref. 17
Steam & hot-press	No	Scots pine	—	—	—	40, 50, 60	Densified with pores	Ref. 18
Saturated steam & hot-press	No	Hybrid poplar	—	—	—	~60	Densified with pores	Ref. 19
Chemical modification & hot-press	Yes	Basswood	52	587	11.5	~80	Densified without pores	Our work
	Yes	Oak	122	608	5	~70	Densified without pores	Our work

Extended Data Figure 6 | Superb mechanical properties of various species of densified wood. Comparison of the stress–strain curve, tensile strength and work of fracture for natural and densified woods of various species: the hardwoods oak and poplar, and the softwoods cedar and pine. **a–c**, Oak (natural wood strength, 115.3 ± 10.2 MPa; densified wood strength, 584.3 ± 29.8 MPa; natural wood work of fracture, 1.84 ± 0.1 MJ m^{-3}; densified wood work of fracture, 5.3 ± 0.2 MJ m^{-3}). **d–f**, Poplar (natural wood strength, 55.6 ± 8.0 MPa; densified wood strength, 431.5 ± 15.1 MPa; natural wood work of fracture, 0.48 ± 0.05 MJ m^{-3}; densified wood work of fracture, 3.0 ± 0.1 MJ m^{-3}). **g–i**, Cedar (natural wood strength: 46.5 ± 5.4 MPa; densified wood strength: 550.1 ± 47.4 MPa; natural wood work of fracture: 0.35 ± 0.06 MJ m^{-3}; densified wood work of fracture, 3.3 ± 0.08 MJ m^{-3}). **j–l**, Pine (natural wood strength, 70.2 ± 10.0 MPa; densified wood strength, 536.9 ± 24.7 MPa; natural wood work of fracture, 0.58 ± 0.07 MJ m^{-3}; densified wood work of fracture, 3.03 ± 0.33 MJ m^{-3}). **m**, Comparison of the structural and mechanical properties of the densified wood in this study and other previously reported[10–19] densified wood materials made from different species of natural wood.

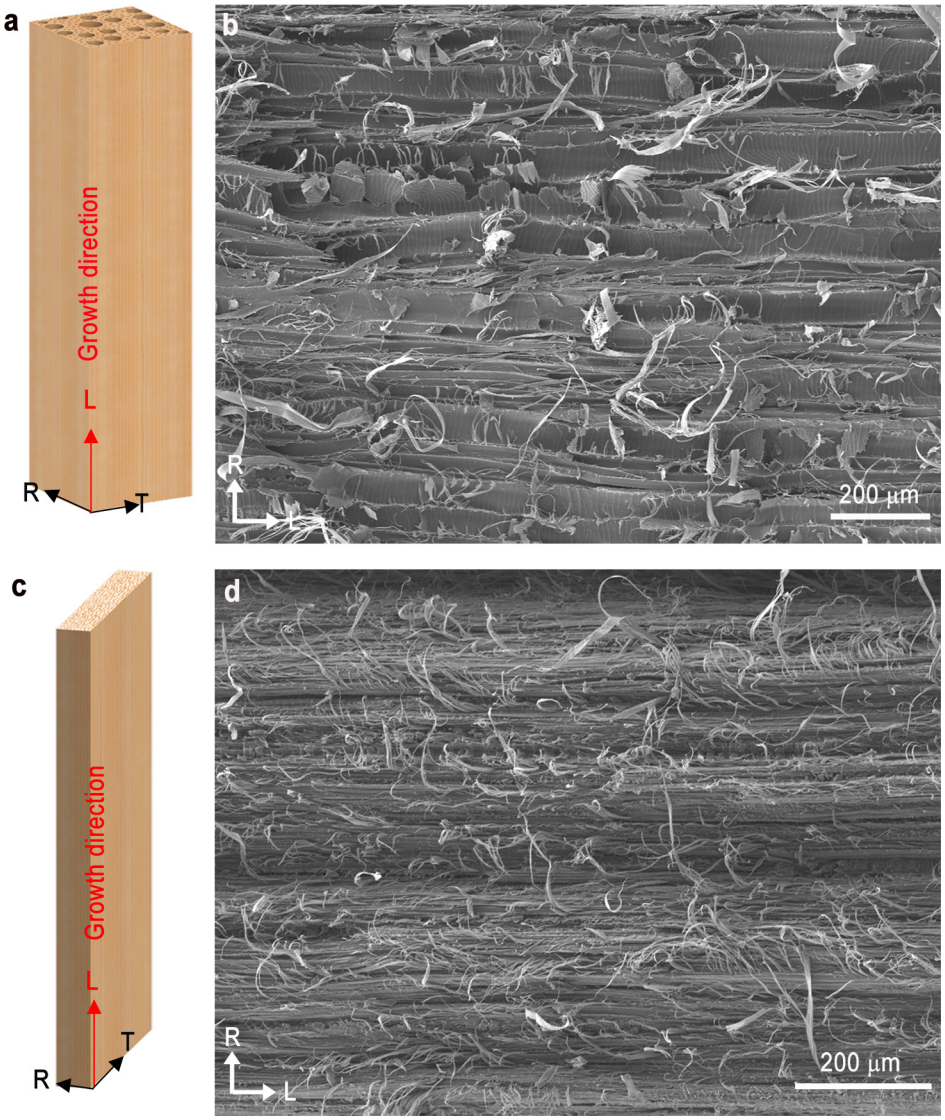

Extended Data Figure 7 | Fracture surface (RL plane) of natural wood and densified wood. a, **c**, The schematics of the natural wood and densified wood. **b**, SEM image of the fracture surface of the natural wood showing the pulling out and tearing of the hollow wood lumina along the fracture surface in the RL plane. **d**, SEM image of the fracture surface of the densified wood in RL plane showing the pulling out and fracture of wood fibres from the densely packed cell walls.

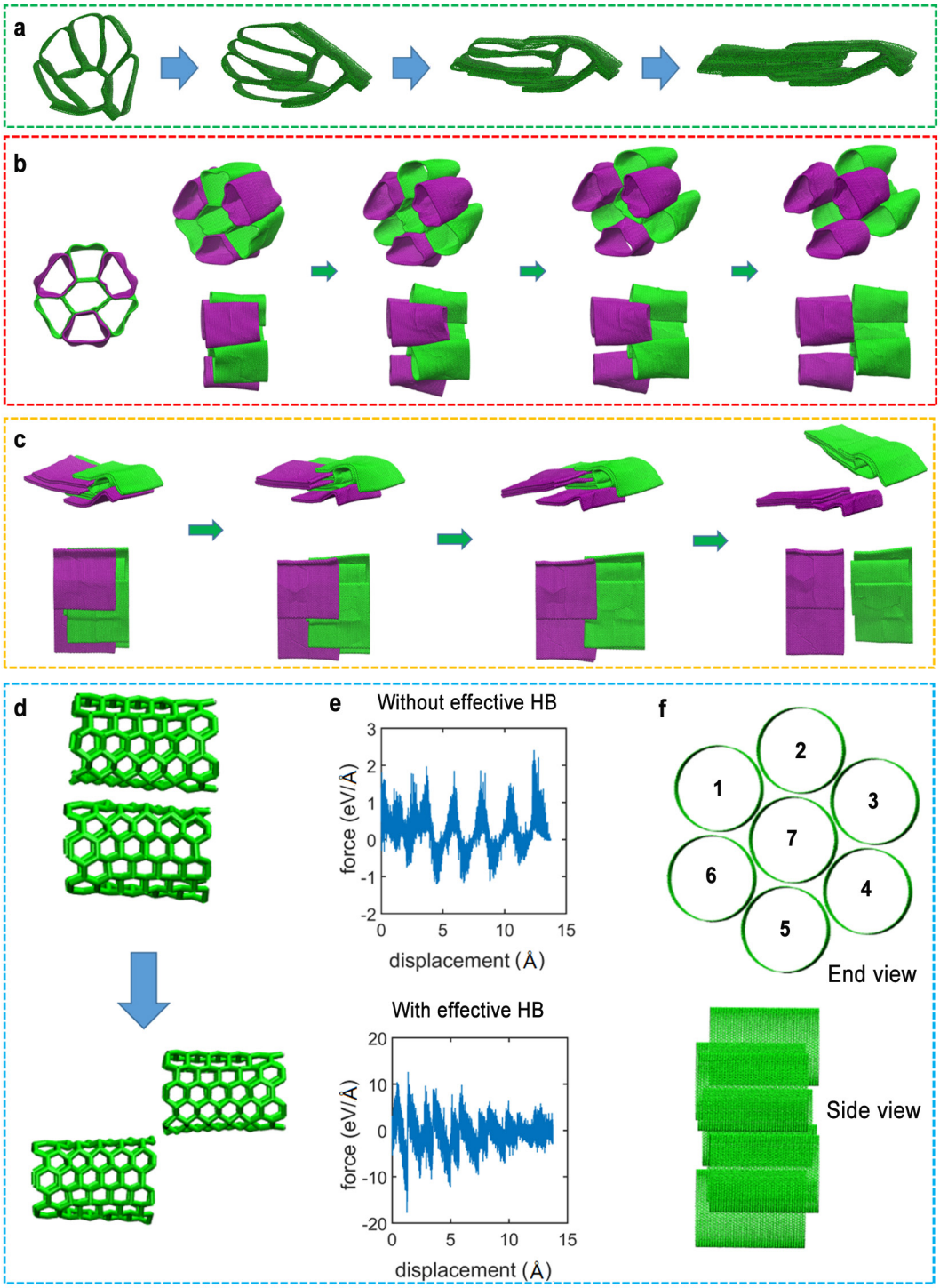

g

r_0	K_{bond}	K_θ	σ	ε	A_n	D_0	α	r_{morse0}
0.142 nm	47.46 eV·Å^{-2}	6 eV	0.2 nm	0.00284 eV	0.2 (same for all n)	1 eV	4.1867 (Å^{-1})	2.245 Å

Extended Data Figure 8 | Simulation model for natural wood and densified wood. a, To obtain the compressed morphology of natural hollow wood fibres in simulations, we apply the reflective wall boundary condition and then gradually shrink one dimension of the simulation box so that the bundle is compressed laterally. **b**, **c**, Morphological view of uncollapsed (**b**) and collapsed (**c**) wood-fibre bundles during pulling. **d**–**f**, Effect of hydrogen bonding (HB). **d**, Simulation model to demonstrate the effect of hydrogen bonding. Two wood fibres slide along each other. **e**, The corresponding resistant forces with hydrogen bonding turned on and turned off (that is, voiding the Morse potential in the simulation force field) are calculated as a function of sliding displacement, respectively, showing that the hydrogen bonding would increase the resistant force by about ten times. **f**, The initial configuration of the seven-lumina bundle model used in the main text. These lumina each have a diameter of 6.26 nm and length of 8.95 nm. **g**, The values of the coarse-grained parameters used in the simulations.

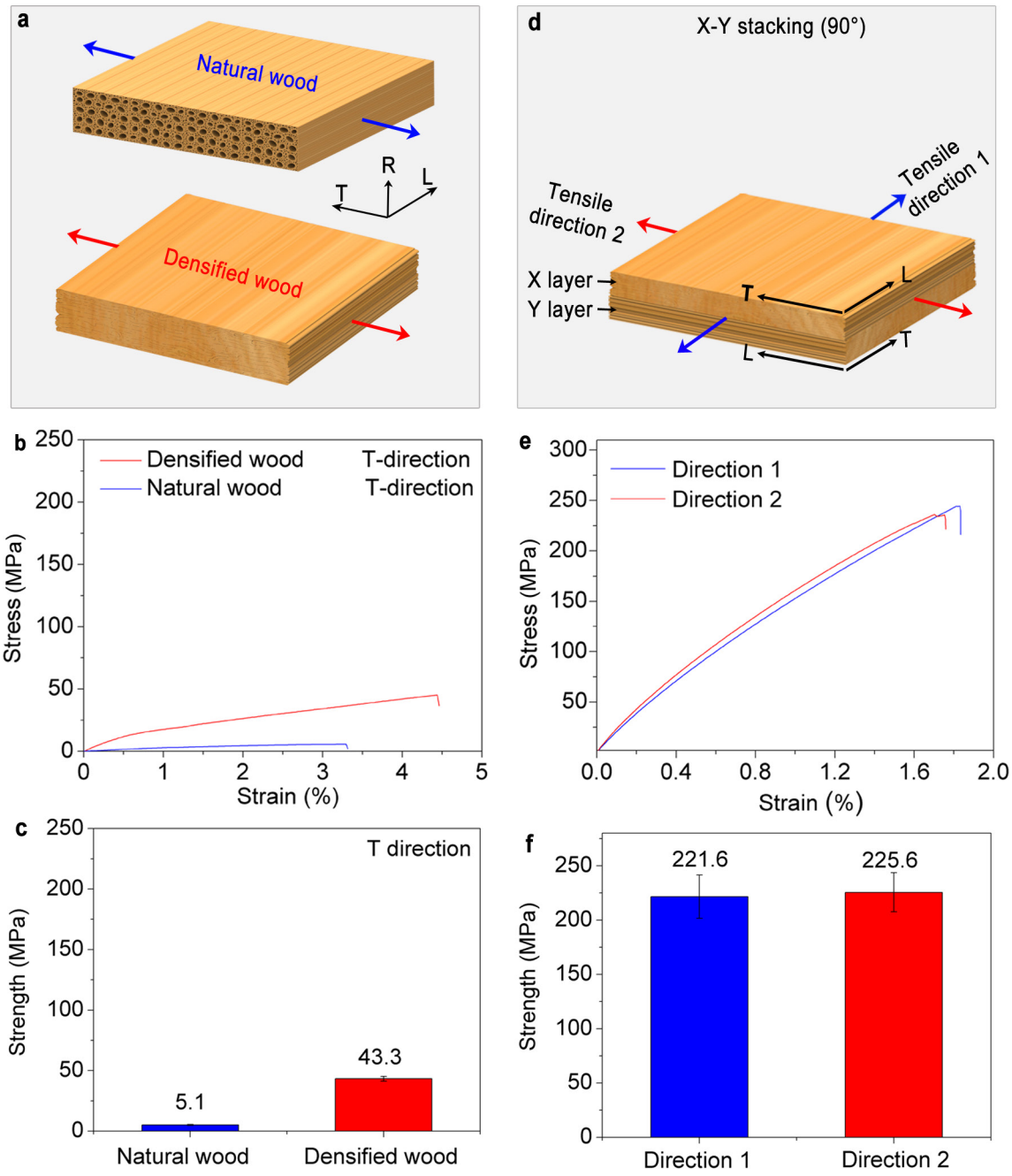

Extended Data Figure 9 | Comparison of tensile properties of X–Y stacking densified wood and monolayer densified wood. a–c, Tensile properties of the natural wood and monolayer densified wood along the T direction: **a**, illustration of tensile direction, **b**, tensile stress–strain curves and **c**, tensile strengths along the T direction (natural wood, 5.1 ± 0.4 MPa; densified wood, 43.3 ± 2.0 MPa). **d–f**, Tensile properties of the X–Y stacking densified wood: **d**, illustration of the X–Y stacking densified wood and two perpendicular tensile directions, **e**, tensile stress–strain curves and **f**, the tensile strengths of the X–Y stacking densified wood along directions 1 and 2 are nearly the same (221.6 ± 20.0 MPa and 225.6 ± 18.0 MPa, respectively), much higher than that of natural wood and that of monolayer densified wood in the T direction.

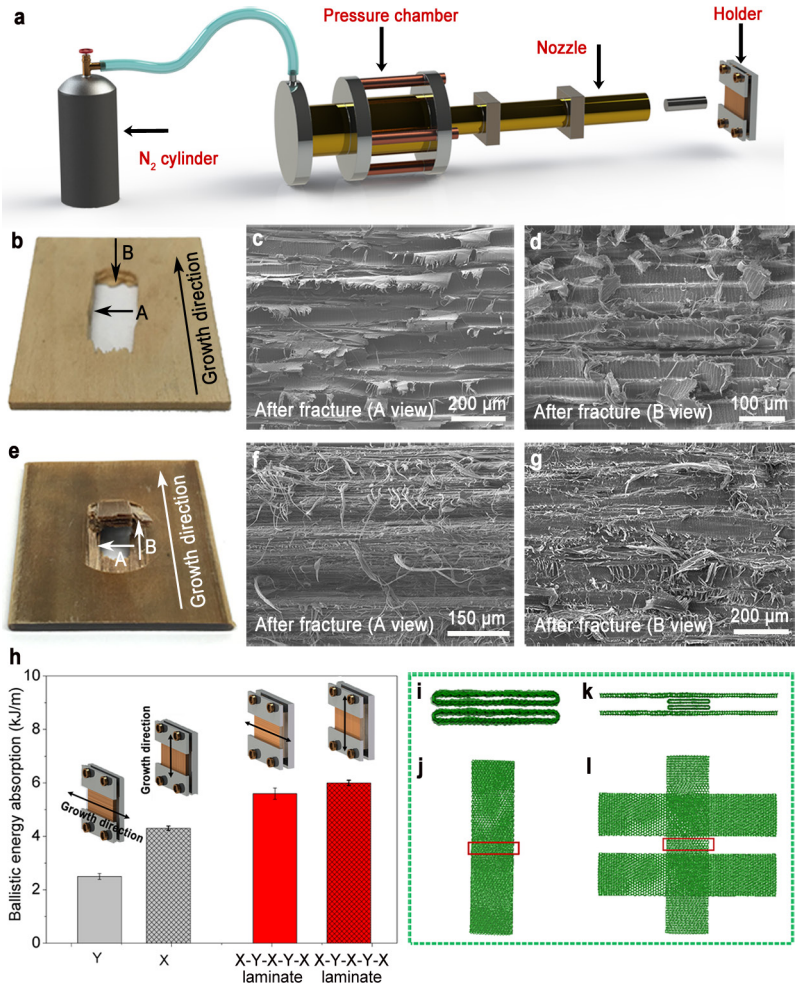

Extended Data Figure 10 | Ballistic test. a, Schematics of the air-gun ballistic tester. **b**, Photograph of natural wood after ballistic test, showing relatively smooth wood surface after the projectile perforates the wood. **c**, **d**, SEM images of the fracture surface show that fracture takes place along the loosely bonded cell walls in natural wood. **e**, Photograph of monolayer densified wood after ballistic test, showing severely chapped wood surface after the projectile perforatesthe wood. **f**, **g**, SEM images of the fracture surface show enormous numbers of wood fibres pulled out from the densely packed cell walls, suggesting substantial energy dissipation during the projectile perforating the densified wood. **h**, Ballistic energy absorption of the monolayer densified wood (Y, 2.5 ± 0.1 kJ m^{-1}; X, 4.3 ± 0.08 kJ m^{-1}) and laminated densified wood (X–Y–X–Y–X laminate: 5.6 ± 0.2 kJ m^{-1}; X–Y–X–Y–X laminate: 6.0 ± 0.1 kJ m^{-1}) from both directions (X, fibre alignment direction; Y, perpendicular to fibre alignment direction). The insets show the schematics of the sample and holder. **i**–**l**, Simulation model used in Fig. 4c, d. **i**, **j**, End view and top view of the parallel wood fibre model, respectively. **k**, **l**, End view and top view of the sandwiched wood fibre model, respectively. These wood fibres (before being collapsed) have a diameter of 2.35 nm and a length of 15.34 nm.